PAPER

# Hydrodynamics of a robotic fish tail: effects of the caudal peduncle, fin ray motions and the flow speed

To cite this article: Ziyu Ren *et al* 2016 *Bioinspir. Biomim.* **11** 016008

Bioinspiration & Biomimetics

PAPER

# Hydrodynamics of a robotic fish tail: effects of the caudal peduncle, fin ray motions and the flow speed

RECEIVED
16 September 2015

REVISED
29 December 2015

ACCEPTED FOR PUBLICATION
18 January 2016

PUBLISHED
8 February 2016

**Ziyu Ren, Xingbang Yang, Tianmiao Wang and Li Wen**

School of Mechanical Engineering and Automation, Beihang University, Beijing 100191, People's Republic of China

**E-mail:** liwen@buaa.edu.cn

**Keywords:** robotic fish, hydrodynamics, locomotion

Supplementary material for this article is available online

## Abstract

Recent advances in understanding fish locomotion with robotic devices have included the use of biomimetic flapping based and fin undulatory locomotion based robots, treating two locomotions separately from each other. However, in most fish species, patterns of active movements of fins occur in concert with the body undulatory deformation during swimming. In this paper, we describe a biomimetic robotic caudal fin programmed with individually actuated fin rays to mimic the fin motion of the Bluegill Sunfish (*Lepomis macrochirus*) and coupled with heave and pitch oscillatory motions adding to the robot to mimic the peduncle motion which is derived from the undulatory fish body. Multiple-axis force and digital particle image velocimetry (DPIV) experiments from both the vertical and horizontal planes behind the robotic model were conducted under different motion programs and flow speeds. We found that both mean thrust and lift could be altered by changing the phase difference ($\varphi$) from 0° to 360° between the robotic caudal peduncle and the fin ray motion (spanning from 3 mN to 124 mN). Notably, DPIV results demonstrated that the caudal fin generated multiple wake flow patterns in both the vertical and horizontal planes by varying $\varphi$. Vortex jet angle and thrust impulse also varied significantly both in these two planes. In addition, the vortex shedding position along the spanwise tail direction could be shifted around the mid-sagittal position between the upper and lower lobes by changing the phase difference. We hypothesize that the fish caudal fin may serve as a flexible vectoring propeller during swimming and may be critical for the high maneuverability of fish.

## 1. Introduction

The analysis of non-traditional biomimetic propulsion swimming under controlled conditions have attracted mathematicians (Alben *et al* 2012), fluid engineers (Anderson *et al* 1998, Barrett *et al* 1999), roboticists (Low and Chong 2010, Wen and Lauder 2013, Wen *et al* 2013, 2014), material engineers (Wang *et al* 2012, Shen *et al* 2013) and biologists' (Wu *et al* 2007, Lauder 2010) interests in studying the principles underlying unsteady locomotion in aquatic animals. The tail of bony fishes is a prominent example of the biomimetic propulsion system, and the caudal peduncle, fin rays and fin membrane together form a dynamic locomotory system during fish swimming (Nauen and Lauder 2002, Flammang and Lauder 2008, 2009). Robotic devices that exhibit a rich variety of dynamic behaviors similar to the fin motions of live swimming fish have allowed for recent advances in understanding the hydrodynamics of caudal fin propulsion (Lauder *et al* 2012). In general, these bio-robotic studies can be divided into two main categories: the first type examined two-dimensional flapping in both the heave and pitch directions in a biomimetic flapping foil that modeled the motion of caudal fin peduncles and investigated hydrodynamic propulsion along the surge direction (Schouveiler *et al* 2005, Akhtar *et al* 2007, Wen and Lauder 2013); the second type employed biomimetic robots with ribbon fins attached to non-moving rigid structures to emulate the fins of bony fish, including knifefish and the Bluegill Sunfish (Curet *et al* 2011, Esposito *et al* 2012, Sefati *et al* 2013).

Based on high-speed images of live swimming fish and the electrical activity of caudal fin muscles, fish fins can exhibit remarkably complex conformational changes during propulsion, and do not function simply as flat plates but have individual mobile fin rays actuated by muscles at the fin base (Lauder and Tangorra 2015). Previous biological studies have demonstrated that three-dimensional fin motion has a great impact on the straight-line steady swimming and horizontal maneuvering of fish (Nauen and Lauder 2002, Flammang and Lauder 2008, Tytell *et al* 2008). For example, a variety of three-dimensional fin kinematics were observed for swimming behaviors such as straight-line steady swimming, accelerating, braking and kick-gliding in Bluegill Sunfish; furthermore, electromyography data showed that red axial myomeres of the caudal peduncle were periodically activated during these behaviors (Flammang and Lauder 2009). These swimming behaviors cannot be achieved through caudal fin ray motion or body undulation alone. The vast majority of fish locomotor patterns utilize both body and caudal fin rays, which are physically connected via the caudal peduncle vertebral joint (Jayne and Lauder 1995). While heave (lateral displacement) and pitch (flexion angle between the midline and the axis of swimming direction) of the caudal peduncle do exist in live fish during locomotion (Jayne and Lauder 1995). From the biomimetic perspective, both caudal peduncle and the fin ray motions should be taken into account when characterizing the hydrodynamic function of the caudal fin system.

Most hydrodynamic studies on the homocercal caudal fin focused on the forces and wake flow of thrust or maneuvering in the horizontal plane using digital particle image velocimetry (DPIV) (Nauen and Lauder 2002, Wu *et al* 2007, Lauder 2015). In contrast, particular attention has been paid to the vertical plane when investigating the hydrodynamic wake flow of heterocercal caudal fin fishes such as sturgeon and shark (Liao and Lauder 2000, Wilga and Lauder 2002, 2004). These studies show that heterocercal-tail fishes have the ability to actively alter the asymmetrical wake flow of their tails when performing vertical maneuvers such as sinking, rising and rotating in the pitch direction. The caudal fin rays of bony fishes, although symmetrical, move in a three-dimensional range and direct water in complex flow patterns in both the horizontal and vertical planes (Esposito *et al* 2012). However, the movement of the caudal peduncle has not been considered when studying the hydrodynamic function of fin ray locomotion.

How do the combined kinematics of the caudal peduncle and fin rays determine the locomotor forces of a caudal fin? What kind of wake flow can be generated by the caudal fin in both the horizontal and vertical planes? Can we use an experimental robotic device to mimic both the caudal peduncle and fin ray motions and to identify an optimal phase relationship between these two? Could the vector forces and wake flow produced by a homocercal caudal fin also play important roles in executing rapid maneuvers during swimming? To our knowledge, no studies have yet addressed the hydrodynamic function of both the caudal peduncle and the fin rays of a homocercal caudal fin, nor developed an experimental robotic system to allow the above questions to be discussed.

In this paper, we designed and fabricated a robotic caudal fin model that mimicked the homocercal tail of the Bluegill Sunfish (*Lepomis macrochirus*), and programmed the robotic model with undulation motions based on data from previous biological studies (Flammang and Lauder 2008, 2009). The robotic model was then mounted to a towing system that could provide heave and pitch that mimicked caudal peduncle motion while the entire model was towed with a precisely controlled speed. DPIV measurements were conducted on both the vertical (mid-sagittal) and horizontal (mid-coronal) planes. Forces, kinematics and wake flow were simultaneously measured at different motion programs and flow speeds. Finally, we discussed the biological relevance of the experimental results and formulated several new hypotheses according to the findings.

## 2. Materials and methods

### 2.1. Biomimetic robotic caudal fin

The Bluegill Sunfish (*Lepomis macrochirus*), a typical ray-finned bony fish performing both active caudal fin surface deformation and body undulatory locomotion during swimming (Flammang and Lauder 2009), was selected as the biological template for the robotic caudal fin. The schematic view of the robotic caudal fin structure was shown in figures 1(a) and (b). The shape of both the fin rays and the streamlined caudal peduncle was designed following the shape of its biological counterpart respectively (Flammang and Lauder 2008), with 90 mm in spanwise length and 170 mm in chordwise length (figure 1(c)). The fin ray was designed to taper from its base to its tip following the shape of a real fish caudal fin (Alben *et al* 2007). The rigid caudal peduncle structure was fabricated with polylactic acid using a fused deposition molding desktop 3D printer (Makerbot replicator2, MakerBot Inc., NY, USA). While the fin rays was fabricated with acrylonitrile butadiene styrene-like rigid material using an Objet Connex500 3D printer (Stratasys Ltd, Eden Prairie, MN, USA). The fin membrane was fabricated with two layers of silicone rubber with thickness of 0.3 mm, and glued with the fin rays using silicone adhesive (ESD Inc., China). The caudal peduncle was rigidly connected to a strut which was mounted to a robotic module that provided heave and pitch motions (figure 2(a)). Each fin ray base was designed as a two degree-of-freedom joint which allowed the fin ray to swing actively and fold passively

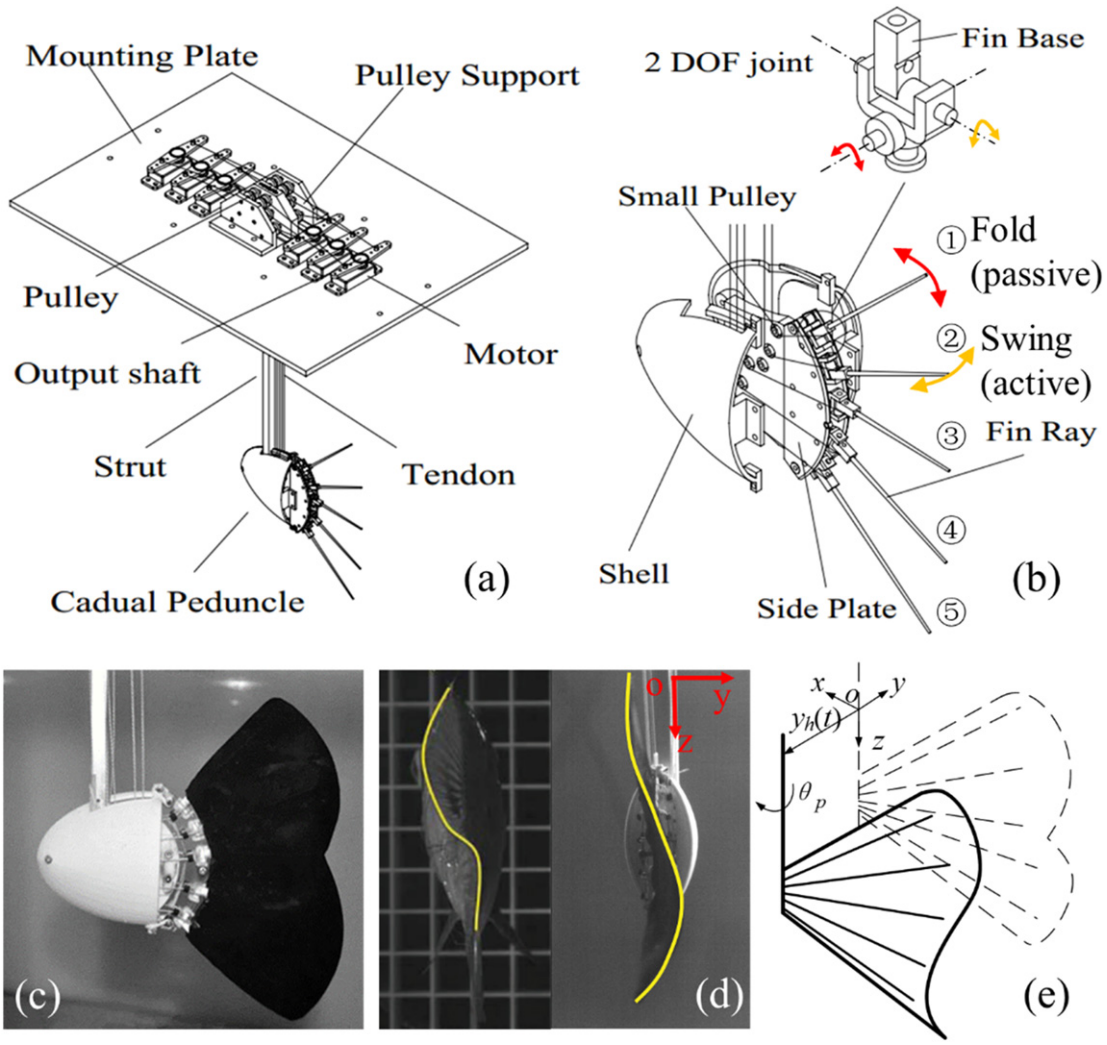


**Figure 1.** Layout of the robotic caudal fin. (a) and (b) demonstration of the robotic caudal fin construction. The fin rays were made to swing (indicated with yellow arrow) by nylon tendons. The tendons were fixed directly to the output shaft of the motors. Fixators were mounted on the motor output shaft to adjust the preload force of the nylon tendons. To reduce drag, a streamlined shell was used. All the low-friction idle pulleys were designed to transmit the nylon tendon movement. The fin rays also had a degree of passive folding (indicated with red arrow). (c) Photo of the robotic caudal fin model. The chordwise direction is along the *x*-axis, while the spanwise direction is along the *z*-axis. Note that the black color was selected for minimizing light reflection from the fin membrane during the DPIV experiments. (d) One frame captured from high-speed video recorded from the posterior view during one flapping cycle for a real fish performing steady swimming (left) (adapted with permission from Esposito *et al* (2012), copyright© The Company of Biologists 2012) and robotic model performing an undulation pattern at $\varphi = 0°$, $U = 0$ cm s$^{-1}$ (right). The yellow curves indicate the trailing edge of the caudal fin. (e) Cartoon demonstration of the peduncle-like heave and pitch motion coupled with fin model in an isometric view.

(figure 1(b)). A tension mechanism was used at each fin ray base to allow the fin membrane to stretch outwards under an appropriate preload stress and fold inwards passively (more details can refer to the supplementary video). Five servo motors (MG995, HuiSheng Inc., China) were used to individually actuate each fin ray. The rotational angle of the motor was controlled by pulse-width modulation signal from a microcontroller STM32ZET6 (STMicroelectronics Inc.). Low-stretch nylon tendon with a diameter of 0.6 mm was used to transmit the movement from the motor to the fin ray base (figure 1(b)), therefore to achieve the swing motion of each fin ray. As the tendons need preloading force to guarantee precision of movements, we used a fixator mounted on the output shaft of the motor that can be used to adjust the preload force before each trial. This tendon-transmission method also allowed all servo motors to be settled above the water surface. More details of our robotic model can be found in our supplementary video.

### 2.2. Kinematics of the caudal fin

Three-dimensional caudal fin movements are commonly observed during Bluegill Sunfish locomotion, and can be labeled as flat, cupping, w-shaped, undulation and rolling (Flammang and Lauder 2009, Esposito *et al* 2012). Among these motions, undulation is considered to generate the largest lift force; therefore, we chose to reproduce undulation in this paper. In this mode, the wave transmits dorso–ventrally, and the

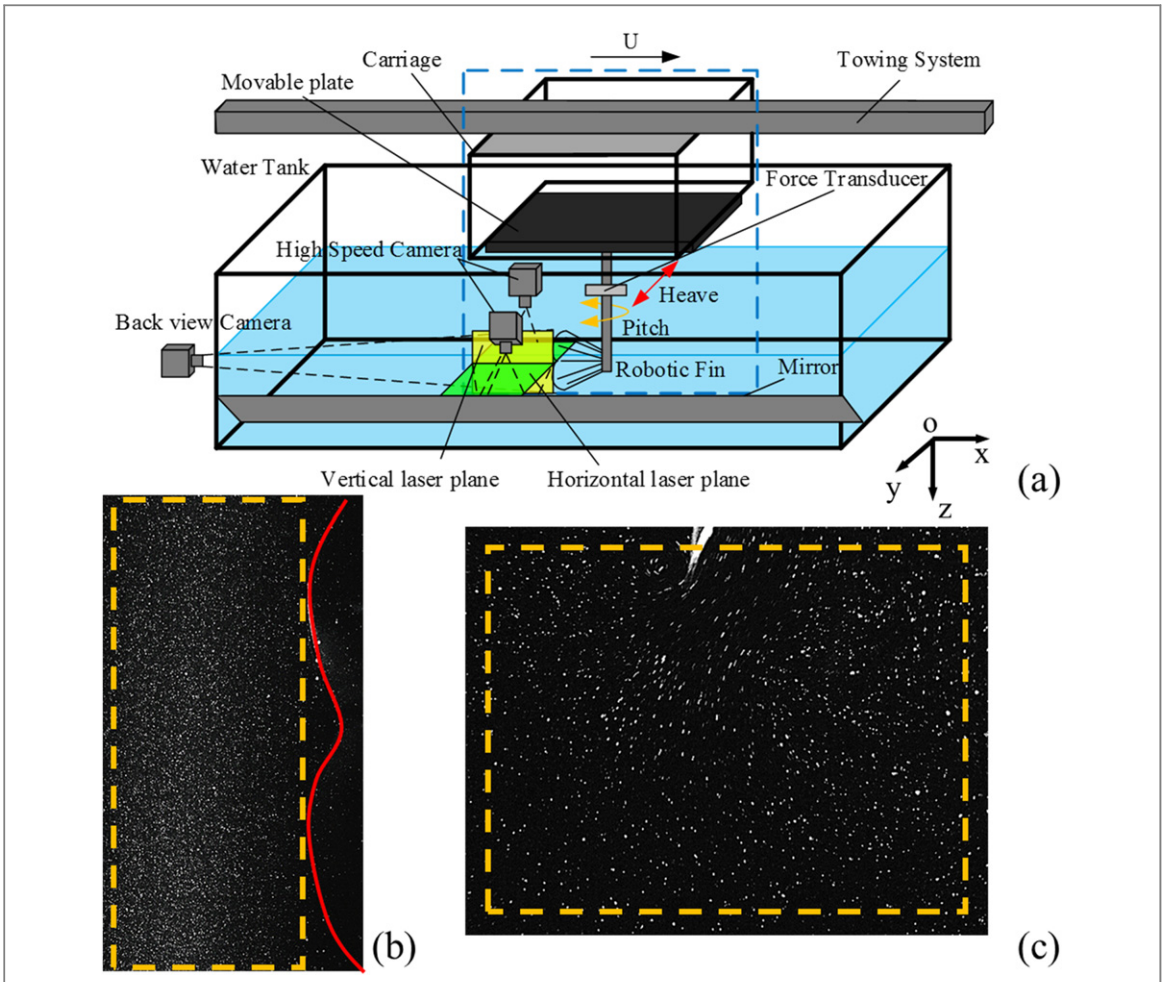


**Figure 2.** Schematic view of the experimental apparatus. (a) The robotic model was mounted on a guide rail system. Heave and pitch were imposed to mimic the caudal peduncle motion. The initial orientation of the caudal fin is in the *xz*-plane. A towing velocity was applied to control the oncoming flow speed. A back view camera was used to record the trailing edge movement. DPIV results and force data can be obtained simultaneously. (b) and (c) high speed camera images of the illuminated particles were collected in the vertical (*xz*, indicated with a yellow plane in panel (a)) and horizontal (*xy*, indicated with a green plane in panel (a)) plane. The red curve indicates the boundary of the trailing edge of the caudal fin. The yellow box marked out the computational domain.

wave amplitude is the maximum lateral displacement of the fin ray tip on the horizontal plane. The wave frequency is equal to that of the fin ray motion. A coordinate system was constructed on a transverse plane of the caudal fin, with the origin (indicated in figures 1(d) and (e) as o) at the projection of the first fin ray tip when the fin is in the initial state (all the fin rays and the fin membrane are aligned on the mid-sagittal plane). The discrete curve equation of the trailing edge can be expressed as:

$$y_{\text{ray}-i}(z,\, t) = -a_u \sin(2\pi ft - 2\pi z/\lambda + \varphi), \quad (1)$$

where $y_{\text{ray-}i}$ is the horizontal displacement of the $i$th fin ray at a certain time $t$ (the numbers of the fin rays are shown in figure 1(b)). $z$ is the ordinate value of the projection of the $i$th fin ray tip in $yoz$ plane. $\lambda$ is the wave length and $\varphi$ stands for the phase difference between the peduncle heave motion and the fin ray motion. The swing angle of the $i$th fin ray base can then be obtained by:

$$\theta_i(t) = \arcsin(y_{\text{ray}-i}(z,\, t)/l_i), \quad (2)$$

where $\theta_i$ and $l_i$ are swing angle and length of the $i$th fin ray, respectively. The robotic caudal fin model was mounted on a movable plate that could provide heave and pitch to imitate the movement of the real fish peduncle (see figure 2 and movie 1). The motion can be expressed as:

$$y_h(t) = -h \sin(2\pi ft), \quad (3)$$

$$\theta_p(t) = p \sin(2\pi ft + \varphi_{hp}), \quad (4)$$

where $y_h$ and $\theta_p$ are heave displacement and pitch angle, respectively. $h$ and $p$ are the heave and pitch amplitude. $\varphi_{hp}$ is the phase difference between the heave motion and the pitch motion. We then need to combine these two movements to determine the resultant displacement of the fin ray tip. If the fin rays keep still and only the peduncle moves, the displacement of the $i$th fin ray tip can be expressed as:

$$y_{\text{peduncle}-i}(t) = y_h(t) + l_i \sin\theta_{ti} \sin\theta_p(t), \quad (5)$$

where $y_h$ and $\theta_p$ can be derived from equations (3) and (4). $\theta_{ti}$ is the angle between the $i$th fin ray and the

horizontal plane. For simplification, we assume $\theta_{ti}$ does not change during the movement and only relates to the morphology of the caudal fin. If the peduncle motion was coupled with the fin ray motion, then the resultant displacement of the $i$th fin ray tip can be expressed as the superimposition of the $y_{\text{ray-}i}$ and $y_{\text{peduncle-}i}$:

$$y_i(t) = y_{\text{ray}-i} + y_{\text{peduncle}-i}. \quad (6)$$

### 2.3. Hydrodynamic experimental apparatus

The experiments were conducted in a tank with length, width and water depth of 7.8 m, 1.2 m and 1 m, respectively (see figure 2(a)). The length of the strut was designed to make the model operate at the middle water depth, minimizing interference from the water surface and the tank bottom. The servo motor of the towing system can provide the robotic model with a precise forward speed ($U$) along $x$-axis. More details about the experimental system can be found in our previous work (Wen *et al* 2012). The movement parameters of the robotic model were set as $a_u = 25$ mm, $f = 1$ Hz, $\lambda = 170$ mm, $h = 15$ mm, $p = 8°$, $\varphi_{hp} = 90°$, which were biologically relevant to its biological counterpart. A series of experiments under different kinematic parameters were then conducted: (a) fin rays moving without caudal peduncle motion (no peduncle motion, $U = 0$ cm s$^{-1}$); (b) caudal peduncle moving without fin ray motion (no fin motion, $U = 0$ cm s$^{-1}$); (c) fin rays and peduncle moving together with different phase differences $\varphi$ (changing $\varphi$ from 0° to 315° with an interval of 45°); (d) fin rays and peduncle moving together with $\varphi = 0°$ under different towing speeds $U$ ($U = 0$, 5, 10 cm s$^{-1}$).

Force data as well as particle images in the vertical plane (mid-sagittal plane, indicated in figure 2(a) with a yellow plane) were recorded simultaneously, and particle images in the horizontal plane (mid-coronal plane, indicated in figure 2(a) with a green plane) were obtained after a simple modification of the guide rail system. The time duration for each trial was limited to 10 s, i.e., ten complete flapping cycles, to avoid violent sloshing in the tank. We measured thrust and lift simultaneously using a multi-axis force transducer (mini-40, ATI Industrial Inc., Canada) with a sample rate of 250 Hz. The mounting position is shown in figure 2(a). The force data were collected by a DAQ card (PCI-6284, National Instrument, Inc., USA). For synchronization, one signal from a motion coordinator (Trio MC206, Trio Motion Technology, UK) triggered the robotic model, servo motors on the guide rail system (providing peduncle and forward motion) and the DAQ card at the same time.

The wake flow patterns were obtained by two-dimensional DPIV flow visualization. The near-neutrally buoyant glass beads with a diameter of 20 $\mu$m were seeded in the water and a laser sheet with a thickness of 1.5 mm was used to illuminate these particles. Particle movements in the vertical and horizontal planes were recorded, and the velocity as well as vorticity fields were then calculated in a subsequent process. The high-speed camera (SP5000, JAI Inc., Denmark) was oriented so that the optical axis was perpendicular to the lightened plane. The sampling rate of the camera was set to 250 Hz to decrease the particle displacement between two frames to an acceptable range, which matched that of the force transducer. The exposure time was set to 2 ms to eliminate overexposure. The raw images of particle movements of two planes are shown in figures 2(b) and (c).

The vortex ring model was described in figure 3. According to Muller *et al* (1997), the impulse $I$ of a vortex ring can be derived from:

$$I = \rho \Gamma \pi R^2, \quad (7)$$

where $\rho$ is the fluid density and $R$ is the vortex ring radius. $\Gamma$ is the circulation of a vortex. From the velocity curve in a body coordinate system, the vortex ring radius $R$ is readily observable (figure 3(d)). We then can obtain $\Gamma$ by calculating the line integral about a curve $C$ enclosing the vortex:

$$\Gamma = \oint_c v_t \, \mathrm{d}x, \quad (8)$$

where d$x$ and $v_t$ are the differential element and the tangential velocity along curve $C$, respectively. The point at which vorticity reaches the largest magnitude was taken to be the 'vortex core'. The curve $C$ was selected to enclose the field where vorticity magnitude was larger than 80% of the vortex core vorticity magnitude.

## 3. Results

### 3.1. Kinematics and hydrodynamic force

We used the kinematic model in equations (1)–(6) for calculating the theoretical trajectory of the trailing edge, and then we compared that with the experimental results. Both theoretical and experimental results of four selected movement patterns are shown in figure 4. It can be observed that the shape of the theoretical model and the curves extracted from the actual experiments agree well with each other. It is also quite obvious that the amplitude of the trailing edge undulation was significantly enhanced when the peduncle motions were applied to fin ray motions. Raw measured force data were processed in LabChart (LabChart 7, ADInstruments Pty Ltd) using a low-pass filter. We conducted three trials for each movement pattern. In each trial, the data of five complete flapping cycles were used to compute the time integral to obtain the mean force of a certain movement pattern under $U = 0$ cm s$^{-1}$. Notably, almost no thrust force was generated without caudal peduncle motion (figure 5(a)). We also found that caudal peduncle motion significantly enhanced the lift force of the caudal fin (figure 5(b)). When caudal peduncle motion

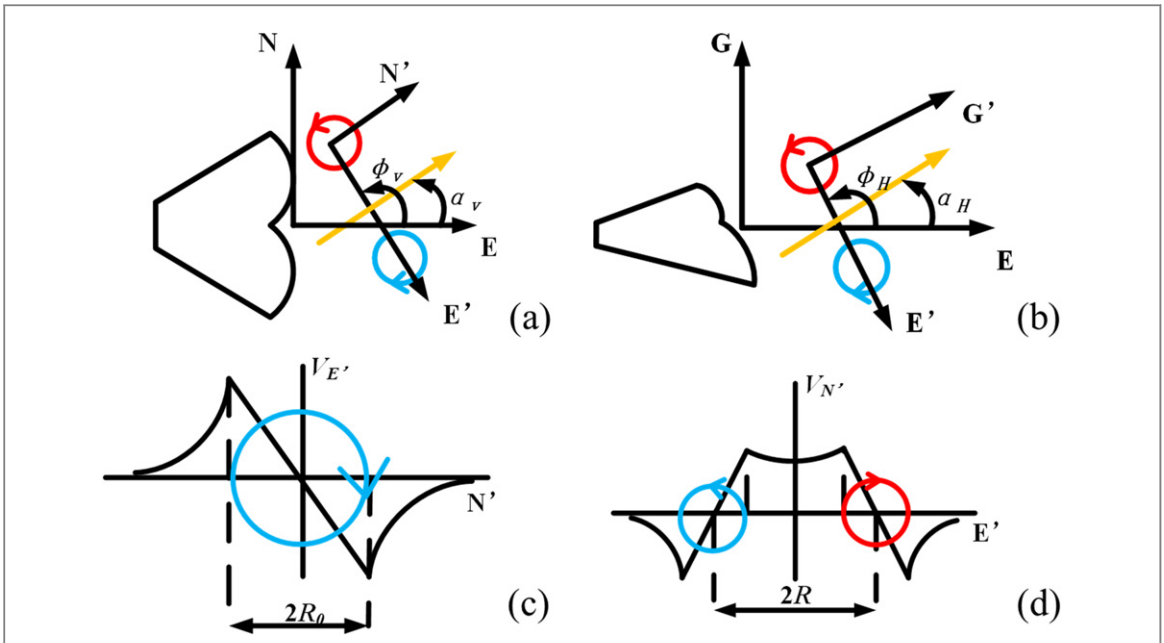


**Figure 3.** Definition of vortex ring morphology in both horizontal and vertical planes. (a) and (b) indicate the schematic view of the vorticity model behind the robot in the vertical and horizontal plane, respectively. The DPIV laser plane illuminated through the vortex ring along the mid-height, and two vortices with an inverse rotating direction and a jet flow (indicated by the yellow arrow) can be observed in both (a) and (b). Global coordinate systems *NE* and *GE* were established on both vertical and horizontal planes for describing the vorticity parameters. Slave coordinate systems *N'E'* and *G'E'* were established for the vortex core and vortex ring model. The vortex ring model was applied to estimate the wake flow field (Muller *et al* 1997, Wu *et al* 2007, Wen *et al* 2012). In this model, a jet will form and pass through a ring-like wake structure. The size of the vortex ring, the vorticity of the vortex core and the angle of the jet will together determine the hydrodynamic impulse. (c) and (d) show the two-dimensional cross section view of the vortex core (with radius of *R*0) and the vortex ring (with radius of *R*), respectively. $\Phi_V$ and $\Phi_H$ are the vortex ring angles in the vertical and horizontal planes, respectively. While $\alpha_V$ and $\alpha_H$ are the jet angles in the vertical and horizontal planes, respectively.

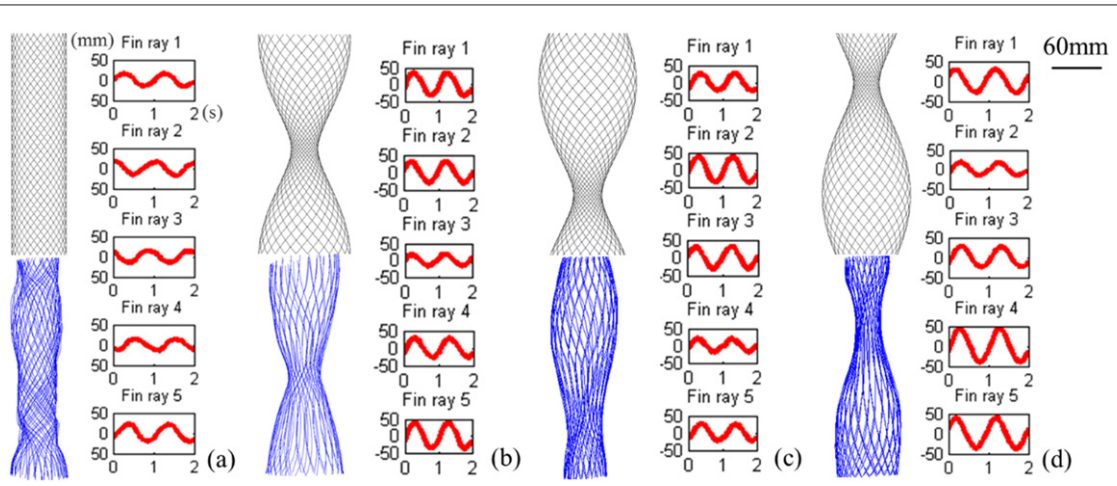


**Figure 4.** Kinematics of the caudal fin trailing edge under different peduncle and fin ray motion programs. Here, we provided the trailing edge trajectories of four movement patterns: (a) fin ray locomotion without peduncle motion; fin ray locomotion with peduncle motion at (b) $\varphi = 0°$, $U = 0$ cm s$^{-1}$, (c) $U = 0$ cm s$^{-1}$, $\varphi = 90°$ and (d) $U = 0$ cm s$^{-1}$, $\varphi = 270°$. The black curves are calculated from the kinematics model, the blue curves indicate averaged experimental results of two motion cycles. Time histories of the five fin ray tips are also provided for each movement pattern, respectively.

was applied, the magnitude of the mean force dramatically increased, even at the minimal thrust generated by the peduncle plus fin ray mode ($\varphi = 45°$). In other experimental cases, the mean lift forces were larger than those generated without fin motion, which resulted in slightly smaller mean thrust. This demonstrates that the three-dimensional fin ray motion has a positive effect on the lift but a somewhat negative effect on the thrust.

When fin rays and the caudal peduncle moved together, the magnitude of the mean thrust and lift were in the same order of magnitude. Under some movement patterns, such as $\varphi = 135°$, lift even surpassed thrust. The value of $\varphi$ has a significant effect on

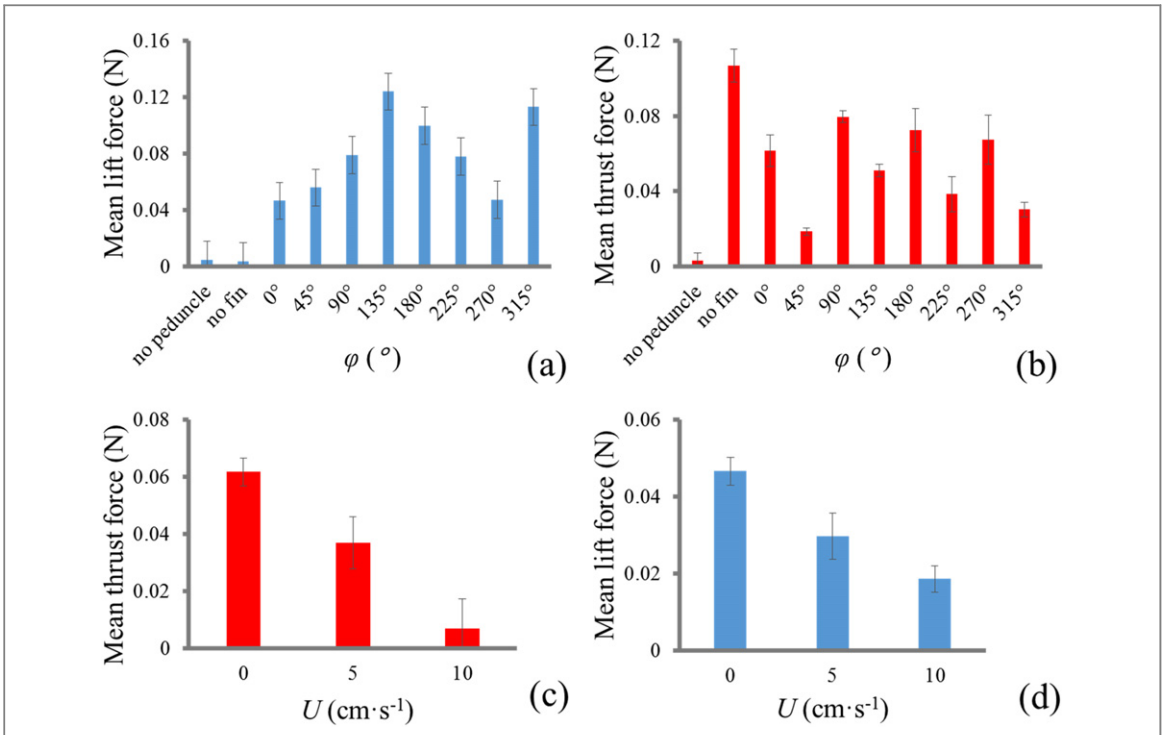


**Figure 5.** Mean thrust and lift generated by the robotic caudal fin. Mean thrust (a) and mean lift (b) during one flapping cycle under different movement patterns (no peduncle motion, no fin motion and the movements under $U = 0$ cm s$^{-1}$, $\varphi = 0° \sim 315°$). Mean thrust (c) and mean lift (d) during one flapping cycle under $\varphi = 0°$, $U = 0, 5, 10$ cm s$^{-1}$. $\varphi$ and $U$ indicate the phase difference and the towing speed, respectively.

the mean thrust and lift. The mean thrust and lift can be modulated within a certain range by changing the phase difference $\varphi$. As $\varphi$ varied, the maximum and minimum thrust appeared at $\varphi = 90°$ and $\varphi = 45°$, respectively, with a maximum–minimum ratio of 4.00. The maximum and minimum lift appeared at $\varphi = 135°$ and $\varphi = 0°$, respectively, with a maximum–minimum ratio of about 2.63.

Experiments at different towing speeds were performed under the conditions of $\varphi = 0°$ and $U = 0$, 5 and 10 cm s$^{-1}$. It can be seen that mean thrust and lift decreased with increased towing speed (figures 5(c) and (d)). Compared with the value at $U = 0$ cm s$^{-1}$, thrust declined 40.3% and 81.3% and lift declined 36.3% and 37.4% under $U = 5$ and $U = 10$ cm s$^{-1}$, respectively. It is not surprising that the thrust decreased, since an increased oncoming flow would induce a larger drag, counterbalancing the thrust and resulting in a lower net thrust. Increased oncoming flow speed also has a remarkably negative effect on lift.

### 3.2. Instantaneous wake flow

The vorticity and velocity fields of the wake flow were obtained by using a commercial flow field analysis software to analyze the DPIV data (LiFangTianDi Inc., China). We found several typical wake structures while running the experimental trials, and selected them for more detailed analysis. The instantaneous wake flow images were created by phase-averaging the vorticity fields over five flapping cycles. Typical wake flow structures on the vertical plane are provided in figure 6, while synchronized instantaneous thrust and lift are shown below the corresponding wake flow images. Without peduncle motion (i.e., fin motion only), a chain of small vortices moves upward ($t = T$). From figure 6(a), it is quite obvious that the magnitudes of both instantaneous lift and thrust without peduncle motion are significantly smaller than those patterns with peduncle motion ($<\pm 0.1$ N). This in turn indicates that little energy was contained in the jet flow while the caudal fin actuated its fin rays without moving the peduncle. The profile of the force curve shows multiple fluctuations, which may be due to the fact that multiple vortices shed during one cycle. Without fin motion (i.e., the caudal peduncle moves while the fin surface remains motionless), a pair of vortices formed an obvious vortex ring with average ring diameter of 37.4 mm (see table 1 for notation) during each flapping cycle at $t = 0.1T$ (figure 6(b)). At this instant, the thrust reached a maximum and the lift reached nearly zero; indeed, every maximum lift corresponded to a minimum thrust. With both peduncle and fin ray motion at $\varphi = 0°$, $U = 0$ cm s$^{-1}$, two separate vortices shed from the upper and lower lobes with jet angles pointed towards the mid-sagittal plane of the caudal fin ($t = 0.56T$, figure 6(c)). At $\varphi = 270°$, $U = 0$ cm s$^{-1}$, two consecutive vortex pairs both shed from the lower lobe moved upward ($t = 0.3T$, figure 6(d)). As evident in figures 6(c) and (d), multiple peaks per cycle occurred in the thrust profiles, while one single peak occurred in the lift profiles. It should be noted that, to our knowledge, no

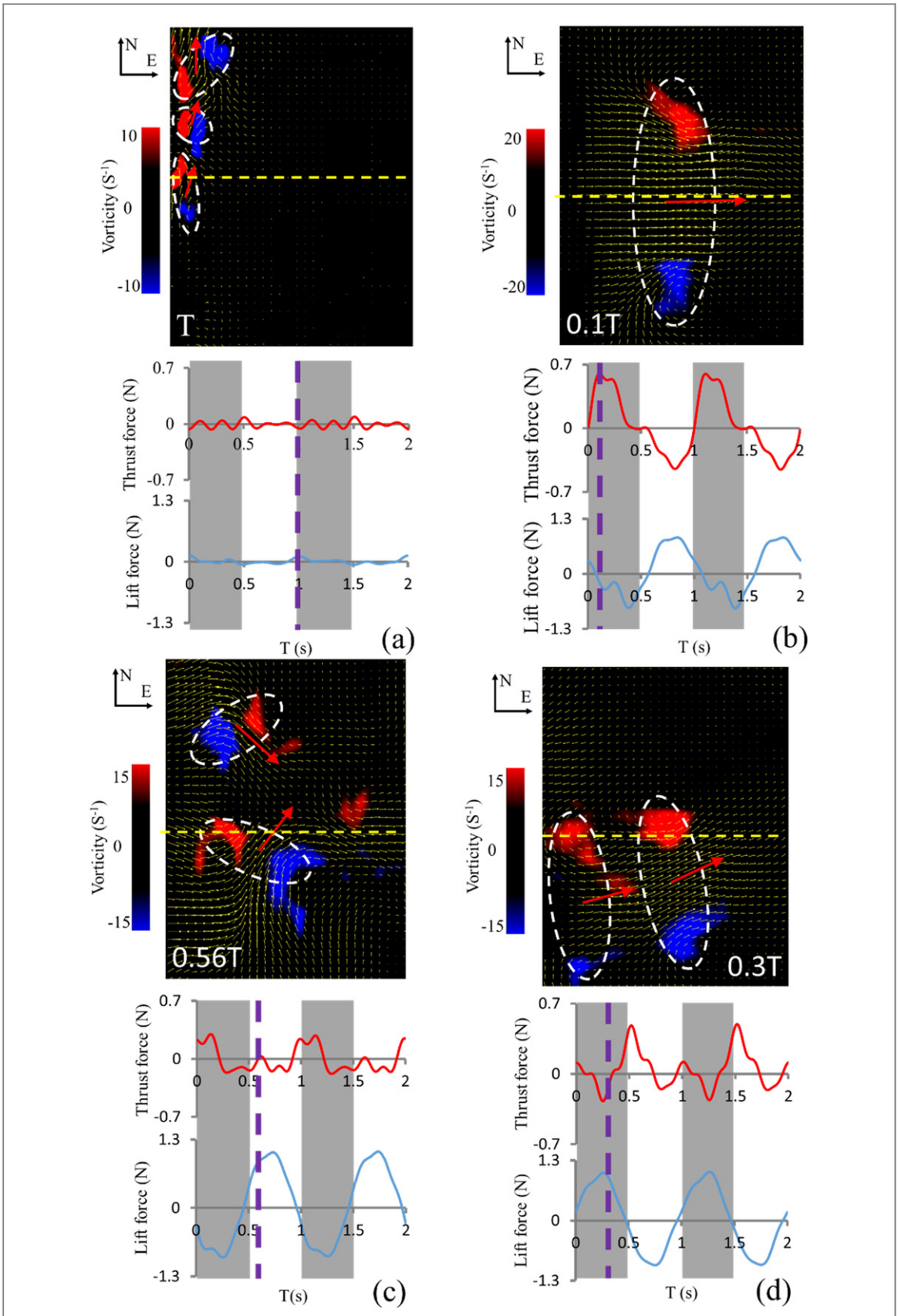


**Figure 6.** Representative instantaneous wake structures of DPIV results in the vertical plane. The yellow horizontal dashed line indicates the position of the coronal plane of the caudal fin. The white dashed ellipse demarcates the vortex pairs. The red arrows show the direction of the jet flow. (a) No peduncle motion, $t = T$; (b) no fin motion, $t = 0.1T$; (c) $\varphi = 0°$, $U = 0$ cm s$^{-1}$, $t = 0.56T$; (d) $\varphi = 270°$, $U = 0$ cm s$^{-1}$, $t = 0.3T$. Instantaneous forces are also given below. The purple vertical dashed line demarcates the instantaneous force at the given time instant.

**Table 1.** Vortex morphological parameters.

| Movement | Plane | Time ($T$) | Mean $R_0$ (mm) | Mean $R$ (mm) | $\Phi_{V/H}$ (deg) | Mean $\Gamma$ (mm$^2$ s$^{-1}$) |
|---|---|---|---|---|---|---|
| No fin motion | Horizontal | 0.66 | 9.30 | 43.07 | 142.80 | 6812.41 |
| | | 1 | 7.17 | 32.41 | 75.74 | 6959.04 |
| | Vertical | 0.1 | 8.95 | 37.38 | 95.41 | 7757.22 |
| | | 0.6 | 10.78 | 20.69 | 104.14 | 4829.11 |
| No peduncle motion | Horizontal | 0.5 | 4.54 | 9.17 | 263.23 | 709.43 |
| | | 1 | 6.61 | 9.01 | 124.92 | 1815.40 |
| | | 0.5 | 3.50 | 6.27 | 225.00 | 1619.74 |
| | | 0.5 | 3.91 | 6.28 | 226.57 | 1850.43 |
| | Vertical | 1 | 7.49 | 8.37 | 188.37 | 2047.32 |
| | | 1 | 2.54 | 3.59 | 143.18 | 1226.78 |
| | | 1 | 6.06 | 8.61 | 98.31 | 1103.92 |
| $\varphi = 0°, U = 0$ cm s$^{-1}$ | Horizontal | 0.12 | 6.49 | 26.84 | 82.55 | 3588.76 |
| | | 0.5 | 7.94 | 15.93 | 111.70 | 4086.53 |
| | | 0.1 | 12.46 | 26.65 | 96.80 | 3506.62 |
| | Vertical | 0.55 | 12.80 | 18.55 | 15.55 | 5401.30 |
| | | 0.55 | 9.20 | 28.37 | 97.94 | 3108.13 |
| $\varphi = 90°, U = 0$ cm s$^{-1}$ | Horizontal | 0.16 | 13.23 | 21.50 | 46.19 | 4966.50 |
| | | 0.66 | 9.28 | 19.98 | 127.91 | 8572.41 |
| | Vertical | 0.22 | 15.02 | 30.03 | 74.03 | 3610.57 |
| | | 1 | 13.10 | 25.85 | 120.76 | 4201.77 |
| $\varphi = 270°, U = 0$ cm s$^{-1}$ | Horizontal | 1 | 17.33 | 32.48 | 48.52 | 7052.72 |
| | Vertical | 0.3 | 9.37 | 25.28 | 94.41 | 4647.54 |
| | | 0.3 | 11.02 | 30.96 | 97.63 | 4385.34 |
| $\varphi = 0°, U = 10$ cm s$^{-1}$ | Horizontal | 0.6 | 8.23 | 48.04 | 162.25 | 8759.69 |
| | | 1 | 11.24 | 39.51 | 64.36 | 9024.32 |
| | | 0.1 | 13.00 | 68.91 | 104.89 | 4744.79 |
| | Vertical | 0.5 | 8.43 | 14.70 | −61.59 | 6082.80 |
| | | 0.5 | 8.91 | 27.89 | 97.94 | 2805.06 |

such wake flow patterns (figures 6(c) and (d)) in the wake flows of swimming fishes or bio-inspired propellers have been reported in previous work.

In the horizontal plane, without fin motion at $U = 0$ cm s$^{-1}$, a typical reverse Karman vortex was observed (figure 7(a)). A wedge-like double vortices can be observed with both peduncle and fin ray motion at $\varphi = 90°$, $U = 0$ cm s$^{-1}$ (figure 7(b)). With the addition of flow speed, a typical reverse Karman vortex with a larger diameter can be observed at $\varphi = 0°$, $U = 10$ cm s$^{-1}$ (figure 7(c)). Without caudal peduncle motion, the vorticity strength decreased dramatically, with tiny visible jet flows with less energy (figure 7(d)). This may in turn indicate that caudal peduncle motion could be critical for generating thrust wake.

We summarize the impulse and jet angles of all typical shedding vortices in figure 8 and table 1. With the addition of fin motion, the absolute jet angles are larger than those without fin motion under most kinetic conditions. On both the vertical and horizontal planes, stronger vortices with larger diameters and impulses were found at $\varphi = 0°$, $U = 10$ cm s$^{-1}$. This in turn suggests that the energy of vortices increased with oncoming flow speed in both the horizontal and vertical planes. However, as the jet angle decreased at the same time, lift declined as well.

### 3.3. Time-averaged wake flow

We plot the time-averaged velocity field by averaging instantaneous velocity fields during one entire flapping cycle. Several typical average wake flow structures in the vertical and horizontal planes are summarized in figures 8 and 9. Velocity components in two directions (i.e., $V_N$ and $V_E$ in the vertical plane, and $V_G$ and $V_E$ in the horizontal plane) on the gray dotted line (15 mm behind the trailing edge) were selected to plot the speed profiles. We found that the phase difference $\varphi$ has a significant effect on the direction of the average flow field. For example, at $\varphi = 0°$, $U = 0$ cm s$^{-1}$, the upper portion of the wake sheds downwards while the lower portion of the fin sheds upwards (figure 9(b)). At $\varphi = 90°$, $U = 0$ cm s$^{-1}$, most of the jet in the wake flow field sheds upwards (figure 9(c)). Notably, the position of the flow shedding also changes with the phase difference $\varphi$. As shown in figure 9(a), with no fin motion flows shed from both the upper and lower lobes of the fin. In the cases of $\varphi = 90°$, $U = 0$ cm s$^{-1}$ (figure 9(c)) and $\varphi = 270°$, $U = 0$ cm s$^{-1}$ (figure 9(d)), however, the shed flows are mainly from the upper and lower lobes, respectively. According to the above results, we hypothesize that the shed point is closely related to $\varphi$: as $\varphi$ increases from 0°, the shed point first begins at both upper and lower lobes ($\varphi = 0°$), then emerges only at the upper lobe

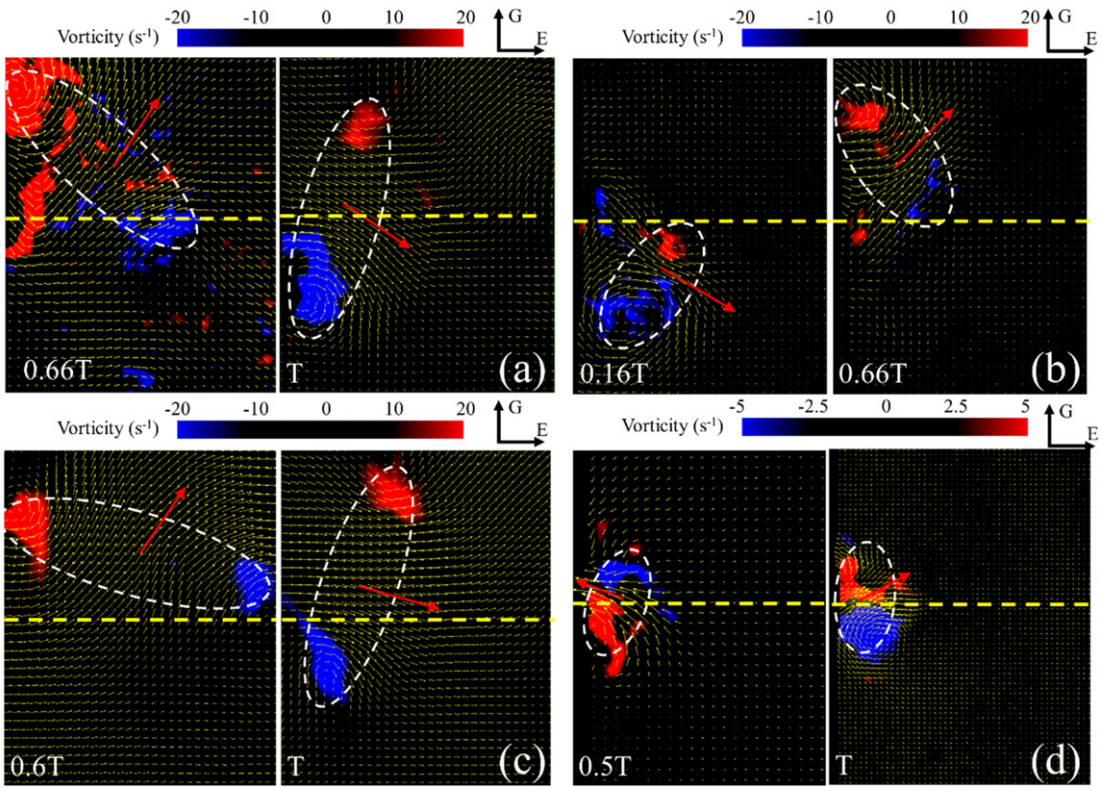


**Figure 7.** Representative instantaneous vorticity field in the horizontal plane. The yellow horizontal dashed line indicates the position of the sagittal plane of the caudal fin. The white dashed ellipse demarcates the vortex pairs. The red arrows show the direction of the jet flow. (a) At no fin motion, noticeable reverse Karman vortexes were formed. (b) At $\varphi = 90°$, $U = 0$ cm s$^{-1}$, wedge like vortexes can be observed. (c) At $\varphi = 0°$, $U = 10$ cm s$^{-1}$, reverse Karman vortexes with larger vortex ring diameter than no fin motion were observed. (d) At no peduncle motion, only tiny vortices with little energy were visible.

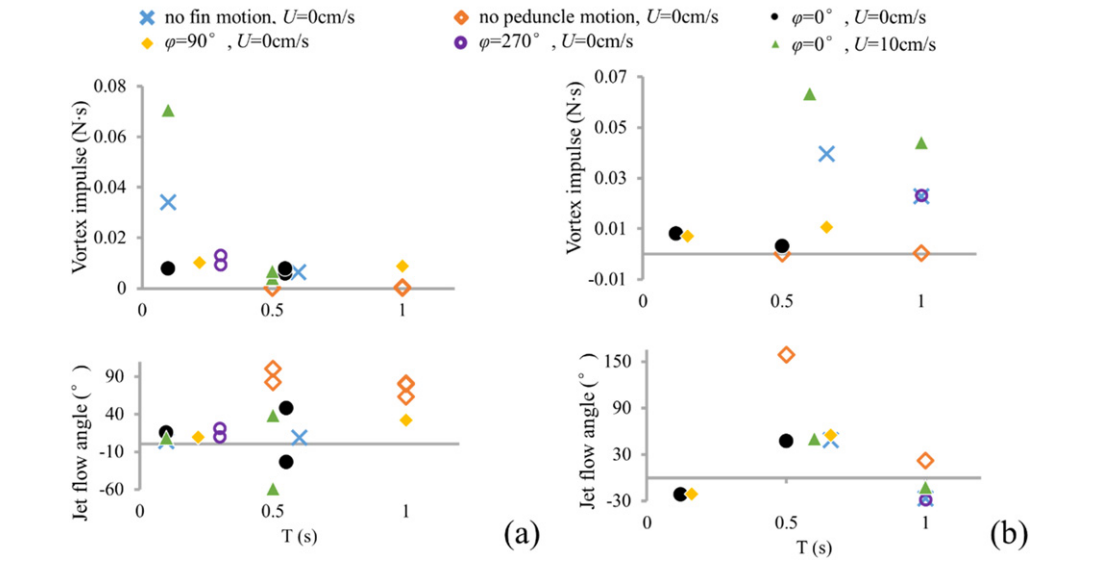


**Figure 8.** Critical parameters of wake structures. Impulse and jet flow angle in (a) vertical plane and (b) horizontal plane are indicated. In both planes, the variation of $\varphi$ changed the shedding time and the jet angle of the vortexes. The increased flow speed ($U = 10$ cm s$^{-1}$) enhanced the vortex impulse significantly, however, decreased the jet angle at the same time.

($\varphi = 90°$). Subsequently it gradually moves downward to the lower lobe ($\varphi = 270°$). Eventually, the vortex shedding from the lower point becomes faint and another new shed point emerges at the upper lobe ($\varphi = 360°$, i.e., $\varphi = 0°$).

We also calculate the ratio of the positive to negative area ($S_+/S_-$, see figure 9). A ratio of 1 indicates that flows shedding from the upper and lower caudal lobes are counter-balanced in the $N$ direction. We found that without fin motion (figure 9(a)), the ratio

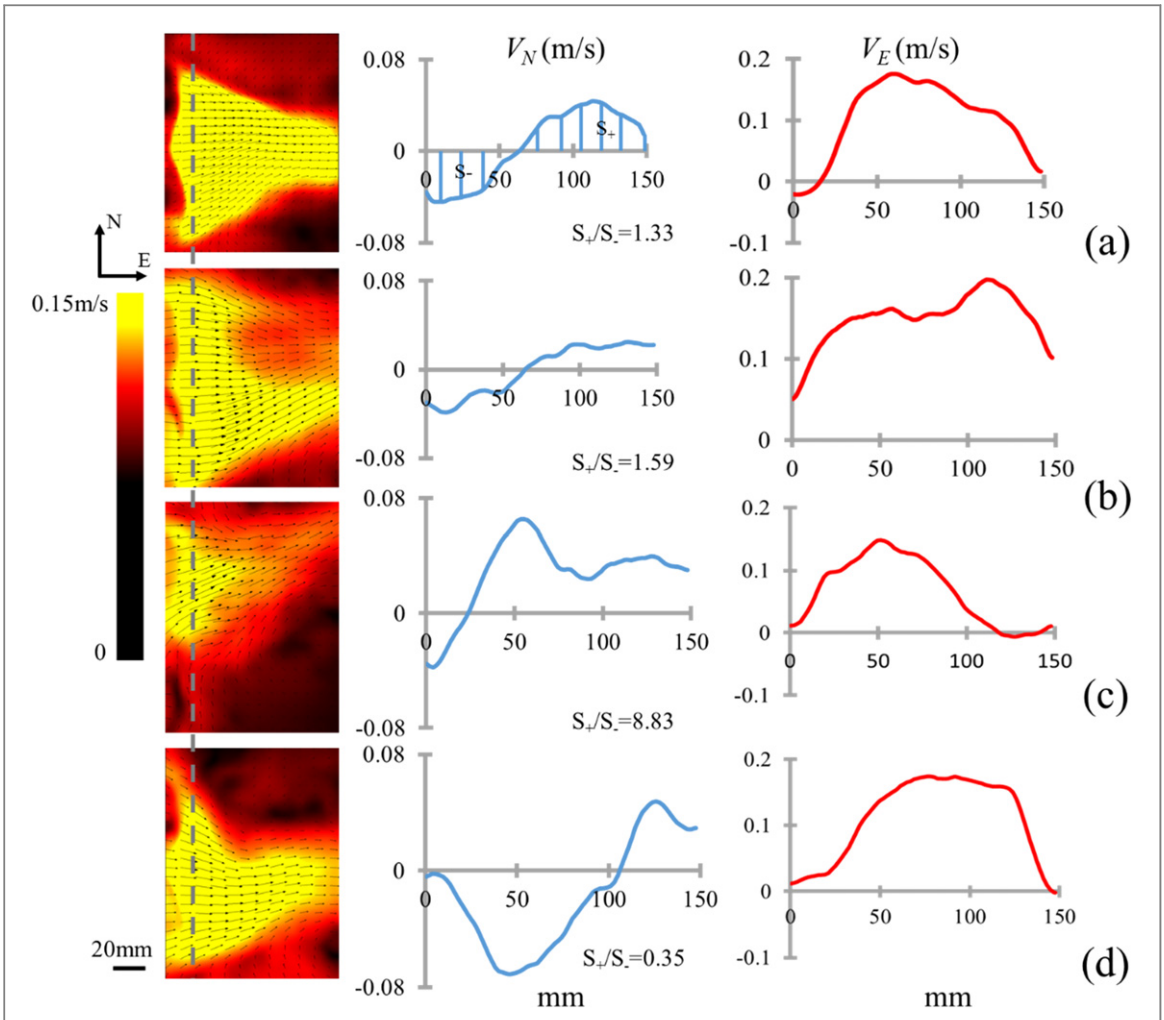


**Figure 9.** Average flow field and velocity curves on gray dotted line in $N$ and $E$ directions at different movement patterns in the vertical plane. (a) No fin motion. (b) $\varphi = 0°$, $U = 0$ cm s$^{-1}$. (c) $\varphi = 90°$, $U = 0$ cm s$^{-1}$. (d) $\varphi = 270°$, $U = 0$ cm s$^{-1}$. The horizontal axis starts from the uppermost point (0 mm) and runs to the lowermost point (150 mm) along the gray dotted line, which has an actual length of 150 mm. The ratio of the positive to negative area ($S_+/S_-$) is also calculated. $S_+/S_- > 1$ indicates more water was pushed upward along the gray dashed line, while $S_+/S_- < 1$ indicates more water was pushed downward along the gray dashed line. Deviation from the value 1 demonstrates that the homocercal tail can also realize functional asymmetry in the vertical direction.

was close to 1 ($S_+/S_- = 1.33$), demonstrating that the flows from the upper and lower lobes were balanced. At $\varphi = 90°$, $U = 0$ cm s$^{-1}$ (figure 9(b)), the upper caudal lobe pushed more water downwards compared to the lower lobe ($S_+/S_- = 1.59$). At $\varphi = 90°$, $U = 0$ cm s$^{-1}$ (figure 9(c)), the upper lobe contributed most of the upward water flow ($S_+/S_- = 8.83$). In contrast, at $\varphi = 270°$, $U = 0$ cm s$^{-1}$ (figure 9(d)), the lower lobe provided a stronger jet compared to the upper lobe ($S_+/S_- = 0.35$). The profiles of the speed along $E$-axis reflect the distribution of the thrust force along the caudal fin trailing edge. The thrust mainly acted on the upper lobe, the lower lobe and the mid-part at the cases of $\varphi = 90°$ (figure 9(c)), $\varphi = 270°$ (figure 9(d)) with $U = 0$ cm s$^{-1}$, and no fin motion pattern (figure 9(a)) respectively. For the case of $\varphi = 0°$, $U = 0$ cm s$^{-1}$ (figure 9(b)), the thrust force seems distributed much more evenly than any other patterns.

The typical average velocity fields on the horizontal plane are shown in figure 10. We found that the wake flow intensity can be significantly changed with $\varphi$. For example, without peduncle motion, the wake flow speeds in both the $V_G$ and $V_E$ directions are significantly smaller than those under other kinetic conditions (figure 10(a)). At $\varphi = 90°$, $U = 0$ cm s$^{-1}$, the wake flow region expanded and the maximum velocity value increased (figure 10(b)). At $\varphi = 0°$, $U = 0$ cm s$^{-1}$, the area of the wake flow region and the maximum velocity achieved maximum values (figure 10(c)). At $\varphi = 90°$, $U = 0$ cm s$^{-1}$, $S_+/S_-$ is 1.76 (figure 10(b)), which was perceptibly smaller than that in the vertical plane (figure 9(c)), indicating that the lateral flow was relatively symmetrical.

## 4. Discussion

### 4.1. Bio-robotic model for understanding biomechanics of fish tail locomotion

For years biologists have suggested that an understanding of the three-dimensional fin motions on the

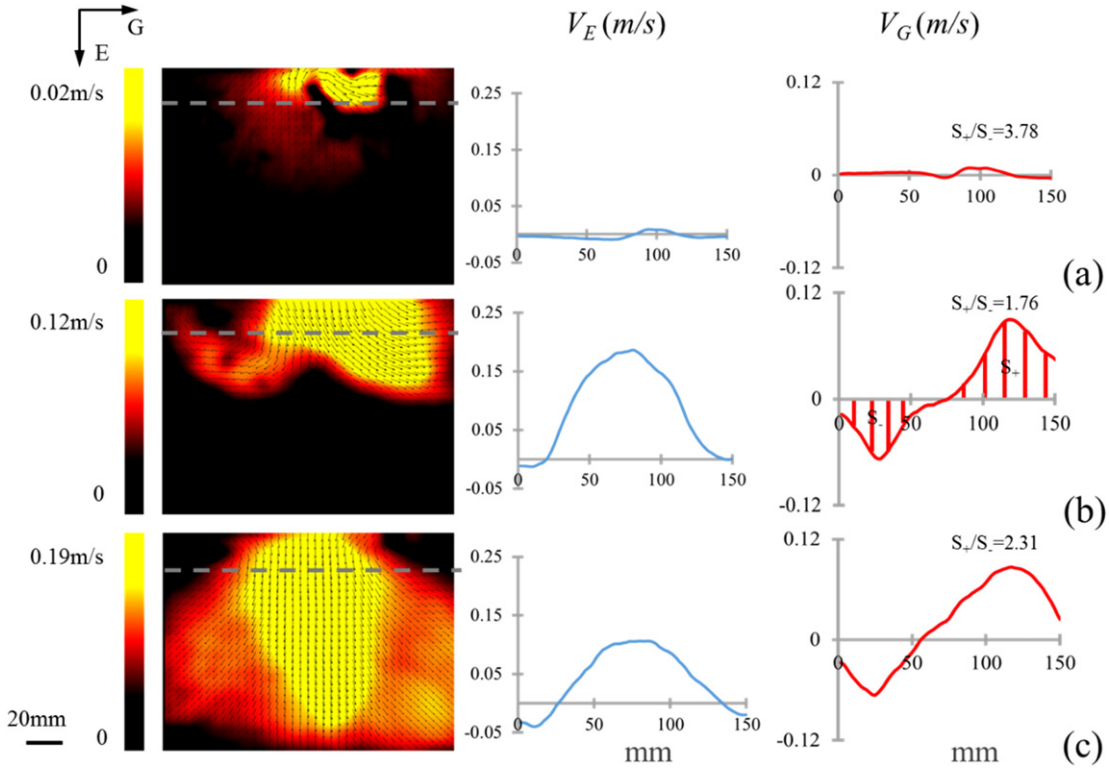


**Figure 10.** Average flow field and velocity curves on gray dotted line in *G* and *E* directions in the horizontal plane. $\varphi$ significantly affects the average wake field. (a) No peduncle motion. (b) $\varphi = 90°$, $U = 0$ cm s$^{-1}$. (c) $\varphi = 0°$, $U = 0$ cm s$^{-1}$. The horizontal axis starts from the leftmost point (0 mm) and runs to the rightmost point (150 mm) along the gray dotted line, which has an actual length of 150 mm. The ratio of the positive to negative area ($S_+/S_-$) is also calculated. $S_+/S_- > 1$ indicates more water was pushed rightward along the gray dashed line, while $S_+/S_- < 1$ indicates more water was pushed leftward along the gray dashed line. Deviation from the value 1 indicates the three-dimensional motion of the caudal fin may cause a slight lateral force and result in rotation as well as a slip motion in the horizontal plane.

undulatory body is vital for explaining the mechanics of fish swimming (Tytell *et al* 2008, Lauder 2010), and they also emphasized that there is an important fact that most fish species use the body and fins at the same time during swimming (Lauder 2015). Bio-robotic fish models have become increasingly important for understanding the biomechanics of fish swimming and formulating new hypothesis, since they can be used to conduct repeatable experiments that are difficult to make with live fish (Lauder 2010). For example, Esposito *et al* have developed a robotic caudal fin model to investigate the effects of fin ray flexural stiffness and motor program on locomotor performance (Esposito *et al* 2012). Curet and Sefati *et al* have developed a biomimetic robot to study the effect of propagating waves on maneuvering forces and wake flow of ghost knifefish swimming (Curet *et al* 2011, Sefati *et al* 2013). Nevertheless, these robotic apparatuses have not yet included the heave and pitch motion that is derived from undulatory fish body, and the effect of the flapping peduncle was not included in the typically described fish tail propulsion system (Triantafyllou and Triantafyllou 1995, Nauen and Lauder 2002, Wilga and Lauder 2002). While in this paper, the fish caudal peduncle movement (heave and pitch motions) was realized by an additional robotic module based on our previous towing system setup (Wen *et al* 2012). Both motions of articulated fin rays and the caudal peduncle could be simultaneously controlled during experiments, thus enabled generating biomimetic motions that mimick the true movement patterns and motion amplitudes of the fin trailing edge (Nauen and Lauder 2002, Flammang and Lauder 2009).

From current experimental results, we did find significantly different kinematics, forces and wake structures compared with previous two-dimensional flapping rigid or flexible foils (Anderson *et al* 1998, Lauder *et al* 2012, Wen and Lauder 2013), and the undulatory fin without attaching to a flapping system (Curet *et al* 2011, Esposito *et al* 2012). The trailing edge kinematics of the robotic fin reflected significant difference between 'with' and 'without' biomimetic caudal peduncle motion (see figure 4 for notation). One noteworthy finding from current hydrodynamic experiment is that the phase difference between the caudal peduncle and fin ray motions enables the fluid forces and wake flow (including jet angle, impulse and wake structure, etc) to be altered in both the horizontal and vertical planes. For example, we demonstrated that the change in phase (phase angle $\varphi$ between the caudal peduncle and the fin ray motion) resulted in

significant variation of kinematics and wake flow, in particular, the hydrodynamic forces (both thrust and lift) varied up to two orders of magnitudes. This outcome, however, could not be achieved through individually manipulating the fin ray motion or the caudal peduncle motion alone (Esposito *et al* 2012, Wen and Lauder 2013).

### 4.2. Hydrodynamic effects of caudal fin peduncle, fin ray motions and the flow speed

Overall, when integrating both the peduncle and fin rays, the phase difference $\varphi$ between the peduncle and fin rays played a critical role in the production of hydrodynamic forces. Specifically, the mean thrust and lift changed harmonically with the phase difference ($\varphi$), with varying ranges of 3 mN–107 mN and 4 mN–124 mN, respectively (see figures 5(a) and (b)). We found that the addition of caudal peduncle motion could greatly change the fin trailing edge kinematics during locomotion, and enhance the thrust and lift forces generated by three-dimensional fin ray motion under certain phases ($\varphi$). The mean thrust force generated by fin ray motion alone without peduncle motion is fairly small (less than 5 mN). With the addition of peduncle motion, the average thrust increased up to 26.3 times ($\varphi = 90°$, $U = 0$ cm s$^{-1}$), and the mean lift increased up to 24.8 times ($\varphi = 45°$, $U = 0$ cm s$^{-1}$). This may be due to the fact that the effect from caudal peduncle led to enlarged fin trailing edge kinematics along the dorsal–ventral direction, therefore the overall hydrodynamic forces were enhanced at appropriate phase $\varphi$ accordingly (see figures 4(c) and (d)). Quite interestingly, compared with peduncle-only motion without fin ray motion cases, all experimental trials integrating fin ray and peduncle movements generated significantly larger mean lifts, but smaller thrusts than those without fin ray motion (see figures 5(a) and (b)). This in turn demonstrates that, with addition of peduncle motion, the fin rays undulation is critical for lift generation, but has a somewhat negative effect on the generation of thrust.

Overall, increased oncoming flow had a negative effect on the generation of lift, and the mean lift decreased dramatically with flow speed, in fact, the lift decreased 60.1% as the flow speed increased from $U = 0$ cm s$^{-1}$ to 10 cm s$^{-1}$ (see figure 5(d) for notation). While increased oncoming flow also enhanced the magnitude of the vorticity shedding, resulting in a larger reactive thrust force: the average vortex momentum in the vertical and horizontal planes in the case of $\varphi = 0°$, $U = 10$ cm s$^{-1}$ was 4–9 times larger than that in the case of $\varphi = 0°$, $U = 0$ cm s$^{-1}$ (see figure 8). Nauen and Lauder found that the thrust force (calculated from horizontal DPIV data) produced by caudal fin of chub mackerel (*Scomber japonicas*, with around 20 cm body length) was 11 mN at 1.2 FL s$^{-1}$ (24 cm s$^{-1}$) (Nauen and Lauder 2002). When chub mackerel swims at speed of 2.2 FL s$^{-1}$ (44 cm s$^{-1}$), thrust force increased up to 48 mN. These data support the point that 'increased flow resulted in a larger reactive thrust force'. With regard to the lift force, vertical lift forces (calculated from vertical DPIV data) of swimming chub mackerel were respectively –1 ± 1 mN at 1.2 FL s$^{-1}$ (24 cm s$^{-1}$) and –1 ± 2 mN at 2.2 FL s$^{-1}$ (44 cm s$^{-1}$), which were essentially identical to zero. Our experimental data show that the lift decreased from 45 mN to around 20 mN when speed increased from 0 cm s$^{-1}$ to 10 cm s$^{-1}$. We predict that further increasing flow speed would result in smaller lift, even zero. Another interesting paper by He and Wardle addressed the effect of flow speed on the body angle to the horizontal body axis (He and Wardle 1986). They found that *S. scombrus* tended to swim with a body angle (to the horizontal body axis) of approximately 0° at the swimming speeds of 0.9–1.2 TL s$^{-1}$. In contrast, when swimming speeds decreased to 0.4–0.8 TL s$^{-1}$, *S. scombrus* tilted its head up reaching body angles as high as 20°. This result in turn reflects the flow speed may affect the body posture of the live fish during swimming as a result of hydrodynamic force. To sum up, above biomechanics studies on live fishes in turn agree with current experimental results based on the robotic model, reflecting the effect of flow speed on both thrust and lift forces of the live fish during swimming.

Our DPIV results showed that besides a reverse Karman vortex and double wedge-like vortices that have been previously reported (Wen *et al* 2012, 2013), several other wake flow patterns that have not yet been reported in previous studies were observed (see section 3.2 for notation). Thus the peduncle motion have a substantial impact on the wake structure generated by the biomimetic caudal fin. Borazjani *et al* have investigated the wake structure near the fish caudal fin by using a three-dimensional computational fluid dynamics (CFD) model (Borazjani and Sotiropoulos 2010, Borazjani and Daghooghi 2013). Although the CFD model developed by Borazjani *et al* did not incorporate the deformation of the caudal fin surface, their simulation results showed that some wake structures such as Karman vortex and wedge-like double vortex were generated by the model, which is in agreement with our current DPIV results.

### 4.3. Effects of caudal fin motion on three-dimensional maneuverability of fish swimming

Homocercal caudal fins are classically viewed as moving symmetrically in the lateral plane (as a homogeneous, stiff, flat plate) and generating only lateral forces and thrust but not lift. Biological and robotic experimental data on the homocercal caudal fin of bluegill sunfish indicate that the fin moves at an acute angle to the horizontal plane with asymmetrical movement of the fin's dorsal and ventral lobes that would generate lift force (Nauen and Lauder 2002, Esposito

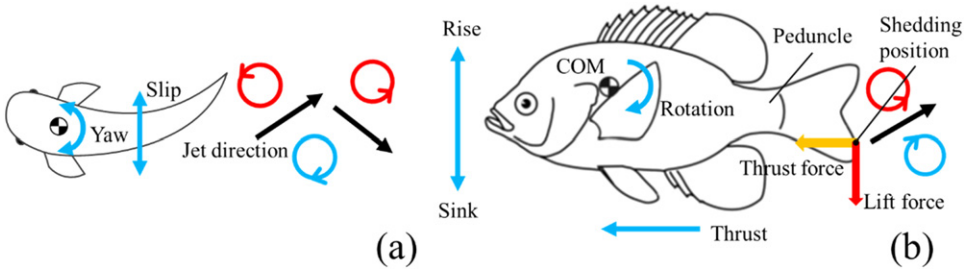


**Figure 11.** Illustration of hydrodynamic forces, vortex rings and the locomotion direction. (a) From the top view, a classic reserve Karman Vortex Street is generated by a swimming fish. Slight yaw and slip motions may also be generated. (b) The center of mass (COM) of a Bluegill Sunfish is located behind the gill. Hydrodynamic force was decomposed into thrust (yellow arrow) and lift (red arrow). The origin, direction and magnitude of force switch with the variation of phase difference $\varphi$, which may induce a significant change in momentum vectors. The force denoted in the chart will result in a downward sink motion, while a forward thrust motion will result in a head-up rotation motion. Adapted with permission from (Tytell *et al* 2008), copyright© The Company of Biologists.

*et al* 2012). Previous studies have already shown that flexible median fins such as anal and dorsal fins function to produce torque and contribute to steady horizontal locomotion, such as the yaw and slip movements shown in figure 11(a) (Tytell *et al* 2008). The DPIV results in our study showed that the significantly differing vorticity magnitudes, shedding points, jet angles and vortex ring impulses can be generated in both the horizontal and vertical planes. These data also suggest that the functional design of fish includes both a flexible body exhibiting undulatory motion and fins that move in three-dimensions and enable fish to vector forces and execute rapid maneuvers.

Although maneuverability can be defined in several ways, it is perhaps most generally recognized as the relative amplitude of the control signal required to change movement direction (Sefati *et al* 2013). That is, if a small change in the control amplitude affects a rapid change in direction, the system would be considered to be highly maneuverable. Note that the caudal fin is located at the far end of the bluegill sunfish with a distance more than 0.5 body length between it and the body center of mass (Xiong and Lauder 2014). Therefore it is quite possible that a small change in force (either lift or thrust) from the caudal fin would contribute to a significant rotational momentum on the fish center of mass. From figure 11(b), the lift generated by the caudal fin provides a clockwise (or counter-clockwise) rotational moment about the center of mass that pitches the body up (or down), increasing the angle of the body to the horizontal body midline and hence the overall fish body would rise up (or sink down). Previous biological studies demonstrated that the sharks can manipulate thrust and lift force by actively altering the stiffness of its heterocercal tail and hence changing the wake behind (Flammang *et al* 2011). Wilga and Lauder also found that the jet flow in vertical plane of the heterocercal tail of leopard shark (*Triakis semifasciata*) and bamboo shark (*Chiloscyllium punctatum*) generated high-angle reaction forces considerably to the center of mass of the shark, which acted to generate torque around the center of mass of the shark (Wilga and Lauder 2002). The heterocercal tail is critical for shark to adjust its body posture during locomotion (Ferry and Lauder 1996) and can move vertically with thrust produced by the tail, sinking or rising in the water even while propelling forward (Wilga and Lauder 2004). Based on previous studies and our experimental results, we cautiously hypothesized that the hydrodynamic forces not only function to provide thrust for fishes, but may also allow for swimming behaviors such as rising, sinking and rotating around the center of mass.

According to the experimental results, we have demonstrated that, the vortex shedding point, the vortex impulse and the jet angle all varied with different $\varphi$ (figures 8 and 9) and generated different mean thrust and lift forces (figure 5). The quantitative vortex morphological parameters show that the vortex jet angle varied from $-23.7°$ to $82.7°$ in the vertical plane. Recalling previous biological studies, leopard shark (*Triakis semifasciata*) and bamboo sharks (*Chiloscyllium punctatum*) generated vortex rings with ring angle ranging from $-35$ to $70°$ during locomotion (Wilga and Lauder 2002). This is very close to our experimental finding. The average velocity fields (figure 9) also show that the wake structure behind the model was very close to that behind a jet vectoring device (Smith and Glezer 2002). Additionally, our experimental results show that, the vortex impulse along the thrust axis changed from nearly 0 to 40 mN s (figures 8), and the vorticity shedding position along the spanwise tail direction can be shifted around the mid-sagittal position between the upper and lower lobes. Therefore we cautiously hypothesize that the hydrodynamic mechanism of the maneuvering control of the fish tail shows a similar strategy to that of a three-dimensional 'vectoring propeller', while maintaining the flexible mechanical property.

## 5. Conclusion

In this paper, we combined fin ray motion with caudal peduncle motion within one bio-robotic model, and investigated how the motion program and flow speed affected the propulsion performance. Experimental data including hydrodynamic forces, average velocity field and vorticity morphology were obtained. These results show that coordinating caudal peduncle and fin ray motions can realize vectored control of hydrodynamic forces. In the future, more advanced technology, such as three-dimensional DPIV, will be applied for a more in-depth understanding of the complex hydrodynamic mechanisms underlying flexible propulsion in fish. In addition to illuminate how a large number of bony fishes can use their tail to move in three-dimensions, the systems using coupled flapping and undulation locomotion provide an emerging technology for future underwater vehicles with high maneuverability. Implementing a complex flexible bio-robotic fish system involving both a body and multiple individual fins will also be a major challenging area of work in the future.

## Acknowledgments

Many thanks to Zhu Qichao, Wang Yueping, and Wang Zaijun for their help in implementing the experimental apparatus and programming motion of the robotic caudal fin. And thanks to Israel Gbati for his help on polishing the article. Particular thanks is given to Hu Kainan who helped to make the video and assisted with data processing. This work was supported by the National Science Foundation support projects, China, under contract number 61403012, National Science Foundation support key projects, China, under contract number 61333016, and Beijing Science Foundation support projects under contract number 4154077.

## References

Akhtar I, Mittal R, Lauder G V and Drucker E 2007 Hydrodynamics of a biologically inspired tandem flapping foil configuration *Theor. Comput. Fluid Dyn.* **21** 155–70

Alben S, Madden P G and Lauder G V 2007 The mechanics of active fin-shape control in ray-finned fishes *J. R. Soc. Interface* **4** 243–56

Alben S, Witt C, Baker T V, Anderson E and Lauder G V 2012 Dynamics of freely swimming flexible foils *Phys. Fluids* **24** 051901

Anderson J M, Streitlien K, Barrett D S, Triantafyllou K and Streitlient D S 1998 Oscillating foils of high propulsive efficiency *J. Fluid Mech.* **360** 41–72

Barrett D S, Triantafyllou M S, Yue D K P, Grosenbaugh M A and Wolfgang M J 1999 Drag reduction in fish-like locomotion *J. Fluid Mech.* **392** 183–212

Borazjani I and Daghooghi M 2013 The fish tail motion forms an attached leading edge vortex *Proc. R. Soc.* B **280** 20122071

Borazjani I and Sotiropoulos F 2010 On the role of form and kinematics on the hydrodynamics of self-propelled body/caudal fin swimming *J. Exp. Biol.* **213** 89–107

Curet O M, Patankar N A, Lauder G V and MacIver M A 2011 Aquatic manoeuvering with counter-propagating waves: a novel locomotive strategy *J. R. Soc. Interface* **8** 1041–50

Esposito C J, Tangorra J L, Flammang B E and Lauder G V 2012 A robotic fish caudal fin: effects of stiffness and motor program on locomotor performance *J. Exp. Biol.* **215** 56–67

Ferry L and Lauder G 1996 Heterocercal tail function in leopard sharks: a three-dimensional kinematic analysis of two models *J. Exp. Biol.* **199** 2253–68

Flammang B E and Lauder G V 2008 Speed-dependent intrinsic caudal fin muscle recruitment during steady swimming in bluegill sunfish, Lepomis macrochirus *J. Exp. Biol.* **211** 587–98

Flammang B E and Lauder G V 2009 Caudal fin shape modulation and control during acceleration, braking and backing maneuvers in bluegill sunfish, Lepomis macrochirus *J. Exp. Biol.* **212** 277–86

Flammang B E, Lauder G V, Troolin D R and Strand T 2011 Volumetric imaging of shark tail hydrodynamics reveals a three-dimensional dual-ring vortex wake structure *Proc. Biol. Sci.* **278** 3670–8

He P and Wardle N C 1986 Tilting behaviour of the atlantic mackerel, *Scomber scombrus*, at low swimming speeds *J. Fish Biol.* **29** 223–32

Jayne B C and Lauder G V 1995 Speed effects on midline kinematics during steady undulatory swimming of largemouth bass, Micropterus salmoides *J. Exp. Biol.* **198** 585–602

Lauder G V 2010 *Animal Locomotion* (Berlin: Springer) pp 3–15

Lauder G V 2015 *Great Transformations in Vertebrate Evolution* (Berkeley, CA: University of California Press) pp 31–45

Lauder G V, Flammang B and Alben S 2012 Passive robotic models of propulsion by the bodies and caudal fins of fish *Integr. Comp. Biol.* **52** 576–87

Lauder G V and Tangorra J L 2015 *Robot Fish* (Berlin: Springer) pp 25–49

Liao J and Lauder G V 2000 Function of the heterocercal tail in white sturgeon: flow visualization during steady swimming and vertical maneuvering *J. Exp. Biol.* **203** 3585–94

Low K H and Chong C W 2010 Parametric study of the swimming performance of a fish robot propelled by a flexible caudal fin *Bioinsp. Biomim.* **5** 046002

Muller U K, van den Heuvel B L E, Stamhuis E J and Videler J J 1997 Fish foot prints: morphology and energetics of the wake behind a continuously swimming mullet (Chelon labrosus Risso) *J. Exp. Biol.* **200** 2893–906

Nauen J C and Lauder G V 2002 Hydrodynamics of caudal fin locomotion by chub mackerel, Scomber japonicus (Scombridae) *J. Exp. Biol.* **205** 1709–24

Schouveiler L, Hover F S and Triantafyllou M S 2005 Performance of flapping foil propulsion *J. Fluid. Struct.* **20** 949–59

Sefati S, Neveln I D, Roth E, Mitchell T R T, Snyder J B, MacIver M A, Fortune E S and Cowan N J 2013 Mutually opposing forces during locomotion can eliminate the tradeoff between maneuverability and stability *Proc. Natl Acad. Sci.* **110** 18798–803

Shen Q, Wang T M, Liang J H and Wen L 2013 Hydrodynamic performance of a biomimetic robotic swimmer actuated by ionic polymer–metal composite *Smart Mater. Struct.* **22** 075035

Smith B L and Glezer A 2002 Jet vectoring using synthetic jets *J. Fluid Mech.* **458** 1–34

Triantafyllou M S and Triantafyllou G S 1995 An efficient swimming machine *Sci. Am.* **272** 64–71

Tytell E D, Standen E M and Lauder G V 2008 Escaping Flatland: three-dimensional kinematics and hydrodynamics of median fins in fishes *J. Exp. Biol.* **211** 187–95

Wang T M, Shen Q, Wen L and Liang J H 2012 On the thrust performance of an ionic polymer–metal composite actuated robotic fish: modeling and experimental investigation *Sci. China Technol. Sci.* **55** 3359–69

Wen L and Lauder G V 2013 Understanding undulatory locomotion in fishes using an inertia-compensated flapping foil robotic device *Bioinsp. Biomim.* **8** 046013

Wen L, Wang T M, Wu G H and Liang J H 2012 Hydrodynamic investigation of a self-propulsive robotic fish based on a force-feedback control method *Bioinsp. Biomim.* **7** 036012

Wen L, Wang T M, Wu G H and Liang J H 2013 Quantitative thrust efficiency of a self-propulsive robotic fish: experimental method and hydrodynamic investigation *IEEE/ASME. Trans. Mechatronics* **18** 1027–38

Wen L, Weaver J C and Lauder G V 2014 Biomimetic shark skin: design, fabrication and hydrodynamic function *J. Exp. Biol.* **217** 1656–66

Wilga C D and Lauder G V 2002 Function of the heterocercal tail in sharks: quantitative wake dynamics during steady horizontal swimming and vertical maneuvering *J. Exp. Biol.* **205** 2365–74

Wilga C D and Lauder G V 2004 Biomechanics: hydrodynamic function of the shark's tail *Nature* **430** 850

Wu G H, Yang Y and Zeng L 2007 Kinematics, hydrodynamics and energetic advantages of burst-and-coast swimming of koi carps (Cyprinus carpio koi) *J. Exp. Biol.* **210** 2181–91

Xiong G and Lauder G V 2014 Center of mass motion in swimming fish: effects of speed and locomotor mode during undulatory propulsion *Zoology* **117** 269–81